

Dark matter stripping in galaxy clusters: a look at the Stellar to Halo Mass relation in the Illustris simulation

Anna Niemiec^{1,2*}, Eric Jullo², Carlo Giocoli^{3,4,5,6}, Marceau Limousin², Mathilde Jauzac^{7,8,9}

¹Department of Astronomy, University of Michigan, 1085 South University Ave, Ann Arbor, MI 48109, USA

²Aix Marseille Univ, CNRS, CNES, LAM, Marseille, France

³Dipartimento di Fisica e Scienze della Terra, Università degli Studi di Ferrara, via Saragat 1, I-44122 Ferrara, Italy

⁴INAF - Osservatorio di Astrofisica e Scienza dello Spazio di Bologna, via Gobetti 93/3, I-40129 Bologna, Italy

⁵Dipartimento di Fisica e Astronomia, Alma Mater Studiorum Università di Bologna, via Gobetti 93/2, I-40129 Bologna, Italy

⁶INFN - Sezione di Bologna, viale Berti Pichat 6/2, I-40127 Bologna, Italy

⁷Centre for Extragalactic Astronomy, Department of Physics, Durham University, Durham DH1 3LE, UK

⁸Institute for Computational Cosmology, Durham University, South Road, Durham DH1 3LE, UK

⁹Astrophysics and Cosmology Research Unit, School of Mathematical Sciences, University of KwaZulu-Natal, Durban 4041, South Africa

Accepted XXX. Received YYY; in original form ZZZ

ABSTRACT

Satellite galaxies in clusters represent a significant fraction of the global galaxy population, and because of the unusual dense environment they live in, their evolution is driven by mechanisms that are different from the ones affecting field or central galaxies. Understanding the different interactions they are subject to, and how they affect them, is therefore an important step towards explaining the global picture of galaxy evolution. In this paper, we use the high resolution hydrodynamical simulation Illustris-1 to study the satellite galaxies in the three most massive host haloes, corresponding to masses $M_{200} > 10^{14} h^{-1} M_{\odot}$. We measure the stellar-to-halo mass relation for the galaxies, and find that it is shifted towards lower halo masses compared to the relation for central galaxies. To explain this shift, we follow the satellite galaxies since their time of accretion in the clusters, and quantify the impact of dark matter stripping and star formation. We find that subhaloes start losing their dark matter as soon as they reach $\sim 1.5 \times R_{\text{vir}}$ from the centre of their host, and that up to 80% of their dark matter content get stripped during infall. On the other hand, star formation quenching appears to be delayed and the galaxies continue to form stars for a few Gyr after being accreted into their host. The combination of these two effects makes the ratio of stellar mass to dark matter mass to vary drastically during infall, going from 0.03 to 0.3.

Key words: Cosmology – Galaxy Clusters – Simulations

1 INTRODUCTION

Clusters of galaxies are the largest gravitationally bound structures in the Universe. In these extremely dense regions, galaxies are subject to violent interactions with their environment and with, both at the level of dark and baryonic matter, which forces them to follow a particular evolutionary path. Many studies show that in the local Universe galaxies

in high density environments are mainly red passive ellipticals (Oemler 1974; Butcher & Oemler 1978; Dressler 1980) and various mechanisms have been identified as having a potential effect on the characteristics of galaxies in clusters: ram-pressure stripping (Gunn & Gott 1972) can remove the galactic gas and thus quench star formation; frequent encounters with other galaxies called harassment (Moore et al. 1996, 1998) can disrupt spiral galaxies into ellipticals; mergers in high density environment may favor the survival of massive galaxies; etc. At the same time, interactions of the

* E-mail: annaniem@umich.edu

dark matter components also drive the evolution of the infalling galaxies. Numerical simulations suggest that dynamical friction sinks galaxies towards the center of clusters, with a strength proportional to the mass of the galaxy (Binney & Tremaine 2008). Concurrently, tidal forces of the host can strip part of the satellite’s matter away, and even disrupt it (Merritt 1983).

Cosmological simulations offer a privileged tool to follow the evolution of galaxies in “real time” and study how they are influenced by the different interactions that they undergo. While progress in computing speed and development of numerical techniques have allowed to model the evolution of the Universe under the cold dark matter paradigm and predict the structure formation scenario (Springel et al. 2005; Klypin et al. 2011), the life and evolution of galaxies remain more demanding to simulate, as they depend on many baryonic processes that act at different scales. Two main techniques have been developed in the past decades to satisfy this need: semi-analytical models (SAMs) or full hydrodynamical simulations.

SAMs (White & Frenk 1991; Kauffmann et al. 1993; Somerville et al. 2008; Guo et al. 2010) rely on dark matter simulations populated with galaxies that evolve following analytical prescriptions motivated by theory or observations. While this approach has quite low computational costs and is quite successful at recovering many statistical properties of galaxies such as the stellar mass function (Guo et al. 2015) or the gas fraction (Somerville et al. 2008), it does not allow to account directly for the interactions of the baryonic and dark matter components. On the other hand, hydrodynamical simulations (Vogelsberger et al. 2014a; Schaye et al. 2015) model the coevolution of dark matter and baryonic matter by coupling gravity with gas physics, and therefore the dynamical processes are more realistically reproduced. They are however requiring much more computational power, which strongly limits their volume: the largest hydrodynamical simulations such as Illustris (Vogelsberger et al. 2014a) or EAGLE (Schaye et al. 2015) now reach ~ 100 Mpc size, while dark matter only universes have been simulated in boxes with side length up to a few Gpc (eg. the Big MultiDark simulation, see Klypin et al. 2016).

As we want to study the coevolution of dark and baryonic matter, the interactions affecting both of them need to be properly examined in the simulation. We use the Illustris simulation which is a hydrodynamical simulation and therefore includes not only gravitational interactions but also gas dynamics and some of the most important astrophysical processes, such as gas cooling, stellar evolution and feedbacks. The Illustris simulation was used to study many different aspects of galaxy evolution, such as their formation (Wellons et al. 2015; Martinović & Micic 2017), structure (Xu et al. 2017) or star formation history (Snyder et al. 2015; Terazas et al. 2016; Bluck et al. 2016). Here we focus on the evolution of galaxies in clusters, and the change in their properties during accretion processes along the cosmic time. Hydrodynamical simulations have proven to be an effective tool to predict the observed properties of satellite galaxies, such as the stellar or subhalo mass function (Bahé et al. 2017), color/quenched fraction (Sales et al. 2015) or spatial distribution (Brainerd 2018), as well as to quantify the mechanisms that lead to them: star formation quenching

(Lotz et al. 2018), matter stripping by gravitational interactions (Smith et al. 2016) or orbital properties (Tormen et al. 2004). In this paper, we focus on the connection between the galaxies and their halo, and how it is modified during infall by processes acting on both the stellar and dark matter components and how it is modified during infall by processes acting on both the stellar and dark matter components.

This paper is organized as follows: in Sect. 2 we present the Illustris simulation; in Sect. 3 we detail our measurements of the stellar-to-halo mass relation for the simulated galaxies (both centrals and satellites); in Sect. 4, we discuss the evolution of galaxies during infall making use of the merger trees for all subhaloes in cluster-like host-halos; in Sect. 5 we quantify the stripping of halos as a function of their distance to the cluster centre; in Sect. 6 we provide a summary and a discussion of our overall analysis. The cosmology used throughout this paper is identical to that used in the Illustris simulation, which is a flat Λ CDM universe consistent with the Wilkinson Microwave Anisotropy Probe 9-year data release (WMAP9, Hinshaw et al. 2013, : $\Omega_{m,0} = 0.2726$, $\Omega_{\Lambda,0} = 0.7274$, $\Omega_{b,0} = 0.0456$, $\sigma_8 = 0.809$, $n_s = 0.963$ and $H_0 = 70.4 \text{ km s}^{-1}$).

2 DATA

2.1 The Illustris simulation

Simulation details. Illustris is a hydrodynamical simulation (Vogelsberger et al. 2014b,a) where dark matter and gas dynamics evolve simultaneously using the moving-mesh code AREPO (Springel 2010), from initial conditions following a Λ CDM cosmology with WMAP-9 parameters (Hinshaw et al. 2013) at redshift $z = 127$, in a comoving box of $75 h^{-1} \text{ Mpc} = 106.5 \text{ Mpc}$ by side. The simulation takes into account different astrophysical processes that drive galaxy evolution, such as gravity, gas cooling and heating, stellar formation and evolution, feedback from stars and supermassive black holes.

Three simulations were run with different resolutions: Illustris-1 (dark matter particle $m_{\text{DM}} = 4.41 \times 10^6 h^{-1} \text{ M}_{\odot}$, baryonic particle $m_b = 8.86 \times 10^5 h^{-1} \text{ M}_{\odot}$), Illustris-2 ($m_{\text{DM}} = 3.53 \times 10^7 h^{-1} \text{ M}_{\odot}$, $m_b = 7.09 \times 10^6 h^{-1} \text{ M}_{\odot}$) and Illustris-3 ($m_{\text{DM}} = 2.82 \times 10^8 h^{-1} \text{ M}_{\odot}$, $m_b = 5.67 \times 10^7 h^{-1} \text{ M}_{\odot}$). The work presented in this paper is based on the most resolved run, Illustris-1. The simulation is sampled in 136 snapshots from $z = 127$ to $z = 0$. The groups are detected with a Friends-of-Friends (FoF) algorithm with linking length $b = 0.2$, and the haloes are extracted using the SUBFIND algorithm (Springel et al. 2001; Dolag et al. 2009) and classified into centrals and satellites from their ranking within their FoF group, so the central halo is generally the most massive subhalo in the group. The snapshot at $z = 0$ contains 4,366,546 SUBFIND groups.

Merger trees. Merger trees have been constructed for all the simulations using two different codes, SUBLINK (Rodríguez-Gomez et al. 2015) and LHALOTREE (Springel et al. 2005). The two algorithms appear to have very similar outcomes and performances (Srisawat et al. 2013), although SUBLINK seems to sometimes be more consistent in subhalo identification during a merger. We therefore chose to use

the SUBLINK merger trees in our analysis. The trees are created as follow. At each time step, a descendant is identified for each subhalo, based on the number of common particles and their binding energy. To avoid losing low mass subhaloes when they cross a structure, SUBLINK allows for one snapshot to be skipped when it looks for descendants. Once all the descendant connections are established the main progenitor of each subhalo is defined as the one with the most massive history behind it.

2.2 Cluster haloes and their subhaloes in the Illustris simulation

In this section we describe the haloes and subhaloes from the Illustris-1 simulation that we use in this work. The Illustris-1 simulation is the most resolved run, with dark matter particle mass $m_{\text{DM}} = 6.3 \times 10^6 M_\odot$ and effective baryonic resolution $m_b = 1.3 \times 10^6 M_\odot$. We therefore select in the Illustris simulation as cluster-like haloes the three most massive systems, that have at $z = 0$ a mass $M_{200} > 10^{14} h^{-1} M_\odot$. This mass selection is for instance equivalent to the redMaPPer cluster selection with richness $\lambda > 20$ (Rykoff et al. 2014; Rozo & Rykoff 2014). We present in Table 1 the main properties of these haloes at the two redshifts of interest, $z = 0$ and $z = 0.35$, where the latter is the mean redshift of the redMaPPer-SDSS clusters which are used to compare our results to observations (e.g. Li et al. 2016; Niemiec et al. 2017). In the next section we compare the Stellar-to-Halo Mass Relation measured for the satellites of these three host haloes to the one measured for all the central galaxies of the simulation (142,720 centrals at $z = 0$ with $M_* > 0$).

Top panel of Fig. 1 shows the mass evolution of the three haloes from $z = 1$ to $z = 0$. It appears that Halo 1 has undergone some violent mass changes in recent times, that could be explained by a major merger. Looking at the mass history of the most massive subhaloes in Halo 1, a recent merger of three haloes of mass $\sim 1 - 5 \times 10^{13} h^{-1} M_\odot$ is indeed identified within the redshift range $z=0-0.4$. It is therefore possible that subhaloes of Halo 1 could experience a different evolution than subhaloes of Halo 0 and Halo 2. We also show in the top panel of Fig. 1 the average mass accretion history predicted from the model in Giocoli et al. (2012, 2013). It is well consistent with the measured evolution of Halo 0 and Halo 2, which have experienced a smooth evolution since $z = 1$, as opposed to Halo 1.

Different estimates of the mass are available for the different objects in the simulation. Following Vogelsberger et al. (2014a), we use galaxy properties defined within twice the stellar half mass radius. The stellar mass is therefore the sum of the mass of all star particles within this radius. We define as stellar mass in central haloes the stellar mass in the central galaxy (another definition could be the sum of all star particle in the halo excluding the subhaloes, we show the stellar mass accretion history for these two definitions in bottom panel of Fig. 1). We show in Fig. 2 the Stellar Mass Function (SMF) for all the central galaxies of the simulation (solid line) and the satellite galaxies of the three host haloes described above (dashed line) at $z = 0$ (blue) and $z = 0.35$ (orange). While the central SMF increases by ~ 0.4 dex between $z = 0$ and $z = 0.35$, the satellite SMF does not evolve much.

For the dark matter content, central haloes are defined

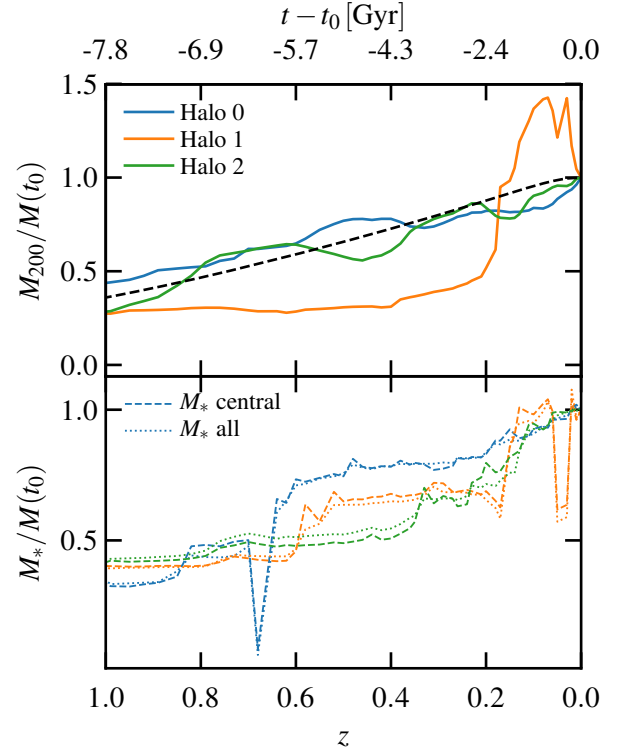


Figure 1. Mass accretion history of the three most massive haloes in the Illustris-1 simulation, with M_{200} on the top panel and the stellar mass on the bottom panel, defined as the central galaxy stellar mass (dashed line), and the mass of all star particles in the halo, excluding the subhaloes (dotted line). The recent brutal mass changes in the accretion history of Halo 1 suggest that it is undergoing a major merger. We show in addition as the black dashed line in the top panel, the average mass accretion history for a halo with $M_{200}(z = 0) = 10^{14} h^{-1} M_\odot$ as predicted from the model in Giocoli et al. (2012, 2013).

as spherical regions with a radius R_{200} , with an average density equal to 200 times the critical density of the Universe $\rho_c(z)$. The mass of the central halo is the total mass contained in this region, M_{200} . For the subhaloes, the mass is defined as the sum of the masses of all particles identified as being gravitationally bound to the subhalo (Springel et al. 2001; Gao et al. 2004; Giocoli et al. 2008, 2010).

3 STELLAR-TO HALO MASS RELATION OF HALOES AND SUBHALOES

3.1 SHMR for central haloes

We now focus on the stellar-to-halo mass relation (SHMR). We first look at the relation for central haloes to provide a comparison point for subhaloes. The relation is shown in Fig. 3: the SHMR is represented for each (central) halo of the simulation, and in addition we compute the median relation in five bins in stellar mass: $10^7 < M_* < 10^8$, $10^8 < M_* < 10^9$, $10^9 < M_* < 10^{10}$, $10^{10} < M_* < 10^{11}$ and $10^{11} < M_* < 10^{12}$, in units of $h^{-1} M_\odot$, and where the small error bars represent the standard error on the median. We show the relation

Halo ID	$z = 0$				$z = 0.35$			
	$\log M_{200}/h^{-1}\text{M}_{\odot}$	$\log M_{*}/h^{-1}\text{M}_{\odot}$	N_{subs}	N_{sub}^{*}	$\log M_{200}/h^{-1}\text{M}_{\odot}$	$\log M_{*}/h^{-1}\text{M}_{\odot}$	N_{subs}	N_{sub}^{*}
0	14.21	12.18	5070	120	14.08	12.08	4113	97
1	14.20	11.99	6756	138	13.76	11.81	1855	33
2	14.19	12.13	5262	112	14.05	11.89	4268	85

Table 1. Properties of the three most massive haloes in the Illustris simulation: mass M_{200} , stellar mass of the central galaxy M_{*} defined as the sum of all star particles within twice the stellar half mass radius, total number of subhaloes N_{sub} and number of subhaloes with $M_{\text{sub}} > 10^{10} h^{-1}\text{M}_{\odot}$ N_{sub}^{*} .

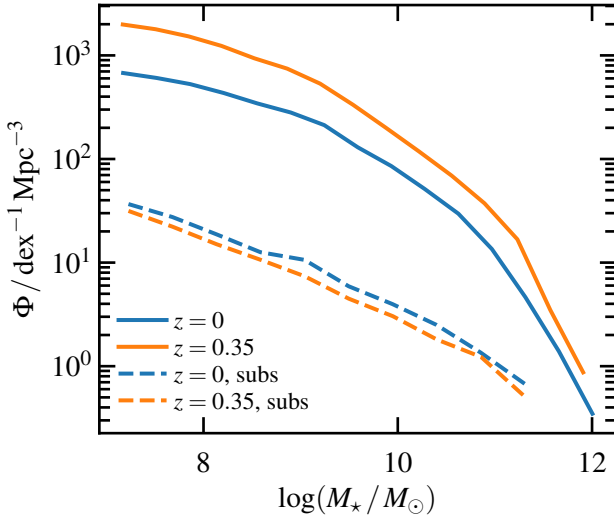


Figure 2. Stellar mass function for all the central galaxies of the Illustris-1 simulation (solide line) and the satellite galaxies of the three most massive haloes (dashed line), at $z = 0$ (blue) and $z = 0.35$ (orange.)

at redshift $z = 0$ and redshift $z = 0.35$, and see no strong evolution between the two redshifts.

We plot in addition the stellar-to-halo mass relation obtained from abundance matching in [Moster et al. \(2013\)](#), defined as:

$$\frac{M_{*}}{M_{200}} = 2N \left[\left(\frac{M_{200}}{M_1} \right)^{-\beta} + \left(\frac{M_{200}}{M_1} \right)^{\gamma} \right]^{-1} \quad (1)$$

where the best fit parameters from [Moster et al. \(2013\)](#) at $z = 0$ are $\log(M_1/\text{M}_{\odot}) = (11.590 \pm 0.236)$, $N = (0.0351 \pm 0.0058)$, $\beta = (1.376 \pm 0.153)$ and $\gamma = (0.068 \pm 0.059)$ (the redshift dependence of the parameters is given in [Moster et al. \(2013\)](#)). We also plot the relation obtained with abundance matching in [Rodríguez-Puebla et al. \(2013\)](#) for central galaxies (we use their results from set C).

These two SHMR differs from our measurements at two mass extrema, and this discrepancy is due to shortcomings on the two sides. It has been shown ([Sawala et al. 2013](#); [Munshi et al. 2013](#)) that SHMR estimated from dark matter only simulations (as in [Moster et al. 2013](#)) overestimate the mass of dark matter haloes, especially at low masses, due to the lack of baryonic physics. However, when correcting for this difference by matching the subhaloes to their counterpart in Illustris DM-only run, the Illustris simulation still appears to overpredict the stellar masses for the most and least mas-

	Priors	Haloes	Subhaloes
$\log M_1/h^{-1}\text{M}_{\odot}$	$[10.5 - 12.5]$	$11.21^{+0.18}_{-0.17}$	$10.66^{+0.35}_{-0.26}$
N	$[0 - 2]$	$0.030^{+0.007}_{-0.006}$	$0.091^{+0.034}_{-0.021}$
β	$[0 - 5]$	$1.27^{+0.13}_{-0.11}$	$0.98^{+0.13}_{-0.12}$
γ	$[0 - 5]$	$0.26^{+0.08}_{-0.08}$	$0.16^{+0.17}_{-0.09}$

Table 2. Priors, best-fit parameters and 68% credible intervals for the parameters M_1 , N , β and γ from equation 1 fitted to the haloes and subhaloes at $z = 0$.

sive haloes ([Genel et al. 2014](#); [Vogelsberger et al. 2014a](#)). At the high mass end, the prediction of overly massive galaxies could be due to insufficient AGN feedback in the Illustris survey (eg. [Vogelsberger et al. 2014a](#)). At the intermediate mass scales, $M_{*} \sim 10^9 - 10^{11} h^{-1}\text{M}_{\odot}$, the two measurements are in good agreement.

We fit the parameters M_1 , N , β and γ from equation 1 to the measured SHMR at $z = 0$. As our galaxy sample is dominated by low-mass objects, we need to weight their contribution. We therefore split the galaxies in 15 bins in $\log M_{*}$, and perform the fit on the median values in each bin, with the $\log M_{*}$ standard deviation in each bin as the error estimate. We obtain the best-fit parameters and the intervals of confidence with a Markov Chain Monte Carlo (MCMC) method using EMCEE ([Foreman-Mackey et al. 2013](#)) which is a Python implementation of an affine invariant MCMC ensemble sampler. The best-fit results with the 68% credible intervals are presented in Table 2, with the flat priors that we used. In addition, we present the joint 2-dimensional and marginalized 1-dimensional posterior probability distributions for the parameters M_1 , N , β and γ in Appendix A. The “normalization” parameters M_1 and N are in reasonable agreement with [Moster et al. \(2013\)](#), but as expected the slopes are different, steeper at high mass and flatter at low mass. We show the SHMR corresponding to our best-fit parameters on Fig. 3. We note that we do not fit the SHMR at redshift 0.35, and simply evolve the relation as in [Moster et al. \(2013\)](#). It seems however that this underestimates the evolution, especially at the mass extrema, as the relation deviates from the measured average points.

3.2 SHMR for subhaloes

We now plot the SHMR for subhaloes in the three cluster-like haloes described in Sect. 2.2. We select all subhaloes except the first ranked one which is the central halo. We plot in Fig. 4 the relation for individual subhaloes and in stellar mass bins, similarly to the SHMR for central haloes.

The SHMR is shifted towards lower halo masses for subhaloes compared to central haloes. We present in Table 3 the stellar and halo masses for each bin, for the central and satellite populations. The error bars represent the standard

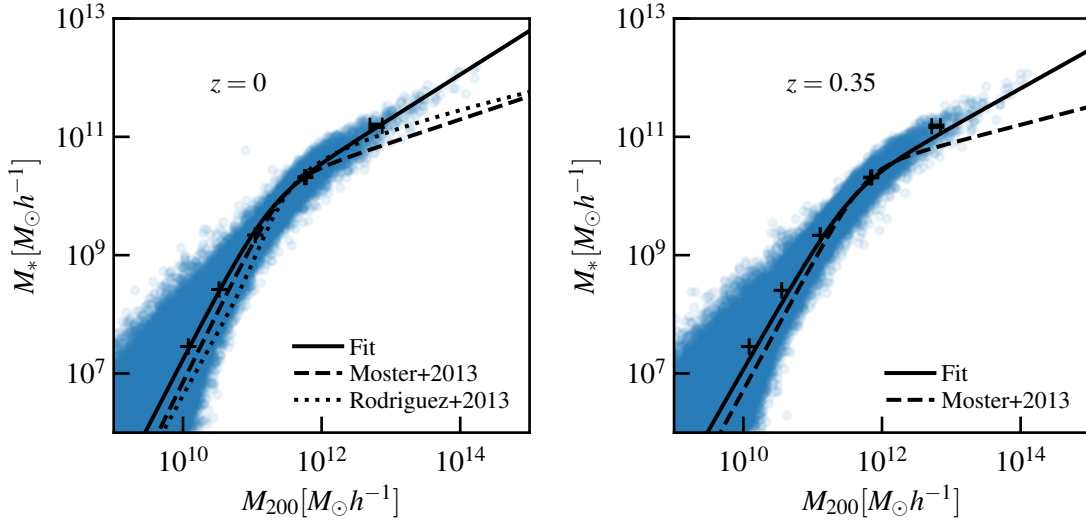


Figure 3. Stellar-to-halo mass relation for haloes from the Illustris-1 simulation. The left panel is for redshift $z = 0$ and the right panel for redshift $z = 0.35$. The masses are expressed in $h^{-1}M_{\odot}$. The blue dots are the SHM ratio for each central halo of the simulation, and the black points are mean values in bins in stellar mass, with error bars that represent the standard error. We plot in addition the relation computed from abundance matching in [Moster et al. \(2013\)](#) for both redshifts (dashed line), and in [Rodríguez-Puebla et al. \(2013\)](#) at $z = 0$ (dotted line).

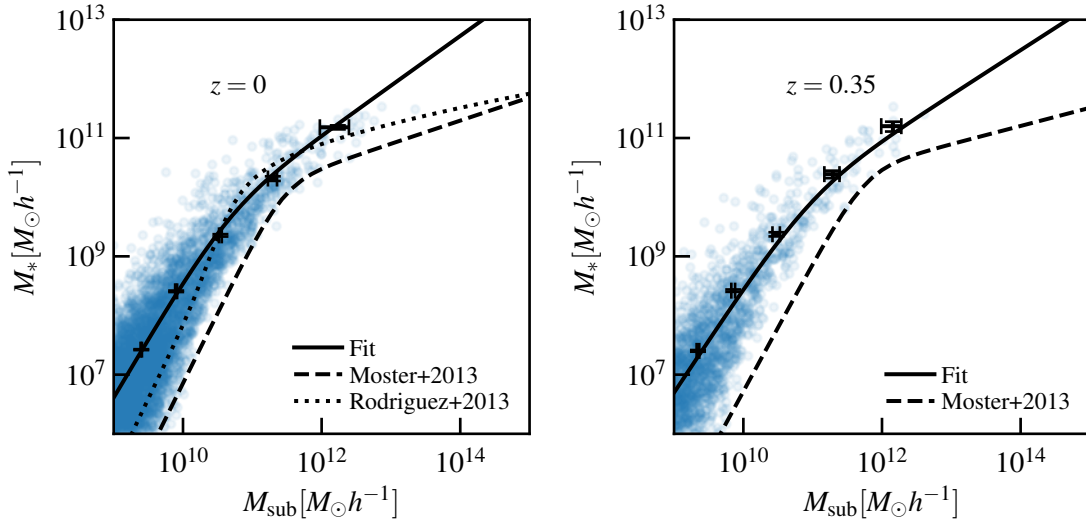


Figure 4. Stellar-to-halo mass relation for sub-haloes of the “cluster like” haloes from the Illustris-1 simulation. The left panel is for redshift $z = 0$ and the right panel for redshift $z = 0.35$. We plot in addition for each case our best-fit relation (solid line) and the relation computed from simulations in [Moster et al. \(2013\)](#) (dashed line). The relation for subhaloes appears to be shifted towards lower dark matter mass compared to the one for haloes. We also plot for $z = 0$ the relation from [Rodríguez-Puebla et al. \(2013\)](#), measured by abundance matching for satellite galaxies and their subhaloes (dotted line).

errors. We fit again the parameters M_1 , N , β and γ from equation 1 using the mean values for the subhaloes at $z = 0$. We show the best fit values and the 68% credible intervals in Table 2, and the posterior probability distributions in Appendix A. We plot the fitted relation as a solid line in Fig. 4. Here again we keep the redshift evolution of the relation as

measured in [Moster et al. \(2013\)](#), and note that it seems to slightly underestimate the evolution that we measure.

The dotted line in Fig. 4 represents the satellite galaxy stellar mass to subhalo mass relation measured by abundance matching in [Rodríguez-Puebla et al. \(2013\)](#). The shift of this relation compared to central galaxies is simi-

M_* bin ($h^{-1}M_\odot$)	$z = 0$		
	$M_{200} \times 10^{-11}$ ($h^{-1}M_\odot$)	$M_{\text{sub}} \times 10^{-11}$ ($h^{-1}M_\odot$)	τ_{strip}
$10^7 - 10^8$	0.119 ± 0.001	0.025 ± 0.001	0.79 ± 0.02
$10^8 - 10^9$	0.331 ± 0.001	0.080 ± 0.003	0.76 ± 0.03
$10^9 - 10^{10}$	1.10 ± 0.01	0.347 ± 0.020	0.69 ± 0.05
$10^{10} - 10^{11}$	5.83 ± 0.21	1.98 ± 0.37	0.66 ± 0.15
$10^{11} - 10^{12}$	62.4 ± 13	17.1 ± 9.6	0.73 ± 0.56
M_* bin ($h^{-1}M_\odot$)	$z = 0.35$		
	$M_{200} \times 10^{-11}$ ($h^{-1}M_\odot$)	$M_{\text{sub}} \times 10^{-11}$ ($h^{-1}M_\odot$)	τ_{strip}
$10^7 - 10^8$	0.121 ± 0.001	0.022 ± 0.001	0.82 ± 0.05
$10^8 - 10^9$	0.358 ± 0.001	0.071 ± 0.006	0.80 ± 0.06
$10^9 - 10^{10}$	1.28 ± 0.01	0.300 ± 0.046	0.77 ± 0.12
$10^{10} - 10^{11}$	6.99 ± 0.24	1.96 ± 0.60	0.72 ± 0.25
$10^{11} - 10^{12}$	61.0 ± 11.0	14.4 ± 5.8	0.76 ± 0.44

Table 3. Mean masses of the central haloes and subhaloes in each stellar mass bin, at $z = 0$ and $z = 0.35$. The stripping factor in each bin is also given.

lar to our measurement at intermediate mass scale ($M_* \sim 10^9 - 10^{11} h^{-1}M_\odot$), but the slopes differ at both mass ends.

Finally, keeping the assumption that the stellar mass does not evolve during accretion and that the “progenitors” of subhaloes of a certain stellar mass are central haloes of the same stellar mass, we define the stripping factor as

$$\tau_{\text{strip}}(M_*) = 1 - \frac{M_{\text{sub}}(M_*)}{M_{\text{h}}(M_*)}, \quad (2)$$

and present the results for each stellar mass bin in Table 3. From this perspective, the stripping factor simply represents the shift in halo mass of the SHMR between central haloes and subhaloes. We plot the evolution of the stripping factor as a function of the mean stellar mass in each bin for $z = 0$ and $z = 0.35$ in Fig. 5. There is no significant evolution with the stellar mass or the redshift. We plot in addition the mean value of the stripping factor $\langle \tau_{\text{strip}} \rangle = 0.75$ and find no significant deviation from it.

We verified that using M_{bound} for the haloes, to have the same dark matter mass definition as for subhaloes, or using $M_{*,\text{bound}}$ for both haloes and subhaloes does not change our conclusions.

4 EVOLUTION SINCE THE TIME OF ACCRETION

In this section, we investigate which mechanisms drive this shift of the SHMR towards lower halo masses for subhaloes. Is the evolution of the dark matter mass at fixed stellar mass completely dominated by tidal stripping? Or is there a contribution from still ongoing star formation? How does the tidal stripping and star formation quenching timescales compare? Is there a significant contribution from mergers? To start answering these questions we will follow the evolution of subhalo properties from the time of their accretion.

We choose again the three most massive haloes of the simulation Illustris-1 (with $M_{\text{h}} > 10^{14} h^{-1}M_\odot$) as cluster-like haloes, and we study the evolution of their subhaloes. We select only the subhaloes with $M_{\text{sub}} > 10^{10} h^{-1}M_\odot$ to guaranty a sufficient number of particles (i.e. $N_{\text{part}} > 280$).

In this section we follow the evolution of the subhaloes with time, by extracting the main branch of their merger trees. We use the merger trees obtained with the SUBLINK algorithm described in Sect. 2.1.

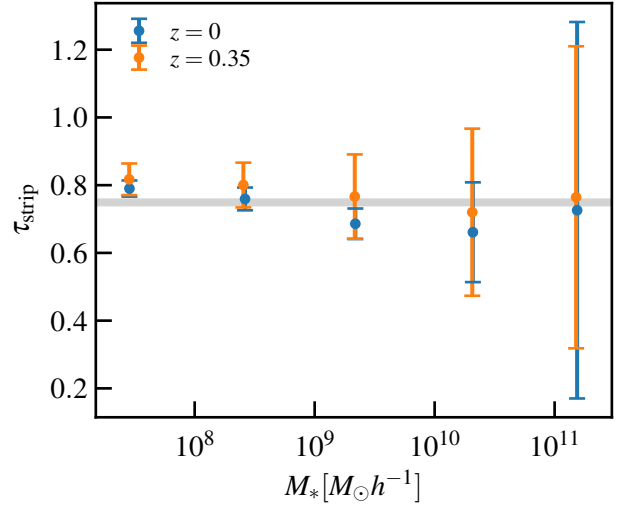


Figure 5. Stripping factor τ_{strip} as a function of the mean stellar mass in each bin, in blue at $z = 0$ and in orange for $z = 0.35$. The grey line represents the mean value.

We need to define a reference time, at which we consider that the halo starts its accretion to the host halo, and starts interacting with it. This accretion time t_{acc} is defined as the moment when the halo enters for the *first* time the shell of radius R_{acc} . We use as the accretion radius twice the virial radius of the host halo $R_{\text{acc}} = 2 \times R_{200}$. Indeed, the cluster extends way outside the virial radius, and its influence on the infalling subhaloes can therefore start before they reach R_{200} . A more physically motivated choice for the accretion radius would be to use the splashback radius (More et al. 2015a; Busch & White 2017; Baxter et al. 2017; Diemer et al. 2017), which is placed by current measurements at around $1.5-2 \times R_{200}$, which motivates our choice of $R_{\text{acc}} = 2 \times R_{200}$.

The subhaloes are then followed within each snapshot after t_{acc} , and the property of interest is plotted as a function of time. In addition, as the measurement of the subhalo mass across the snapshots can be noisy (Muldrew et al. 2011), we perform a sigma-clipping to clean the mass evolution signal.

4.1 Evolution of the halo-centric distance

The first property of interest is the distance between the subhalo and the centre of the host halo. We present in the top panel of Fig. 6 the evolution of the cluster-centric distance normalized by the virial radius of the host halo at the time of accretion, as a function of time since accretion, for each of the three cluster-like haloes separately. Each column corresponds to a host halo. In each panel the black curves represent the evolution for each subhalo independently, and the thick red line the median value at each time step, the thin red lines highlighting the evolution of the 16th and 84th percentiles.

As expected, the subhaloes are moving towards the centre of their hosts, and this ensemble infall motion has already started at $2 \times R_{200}$ from the centre. It is therefore interesting to follow the properties of the subhaloes at this distance,

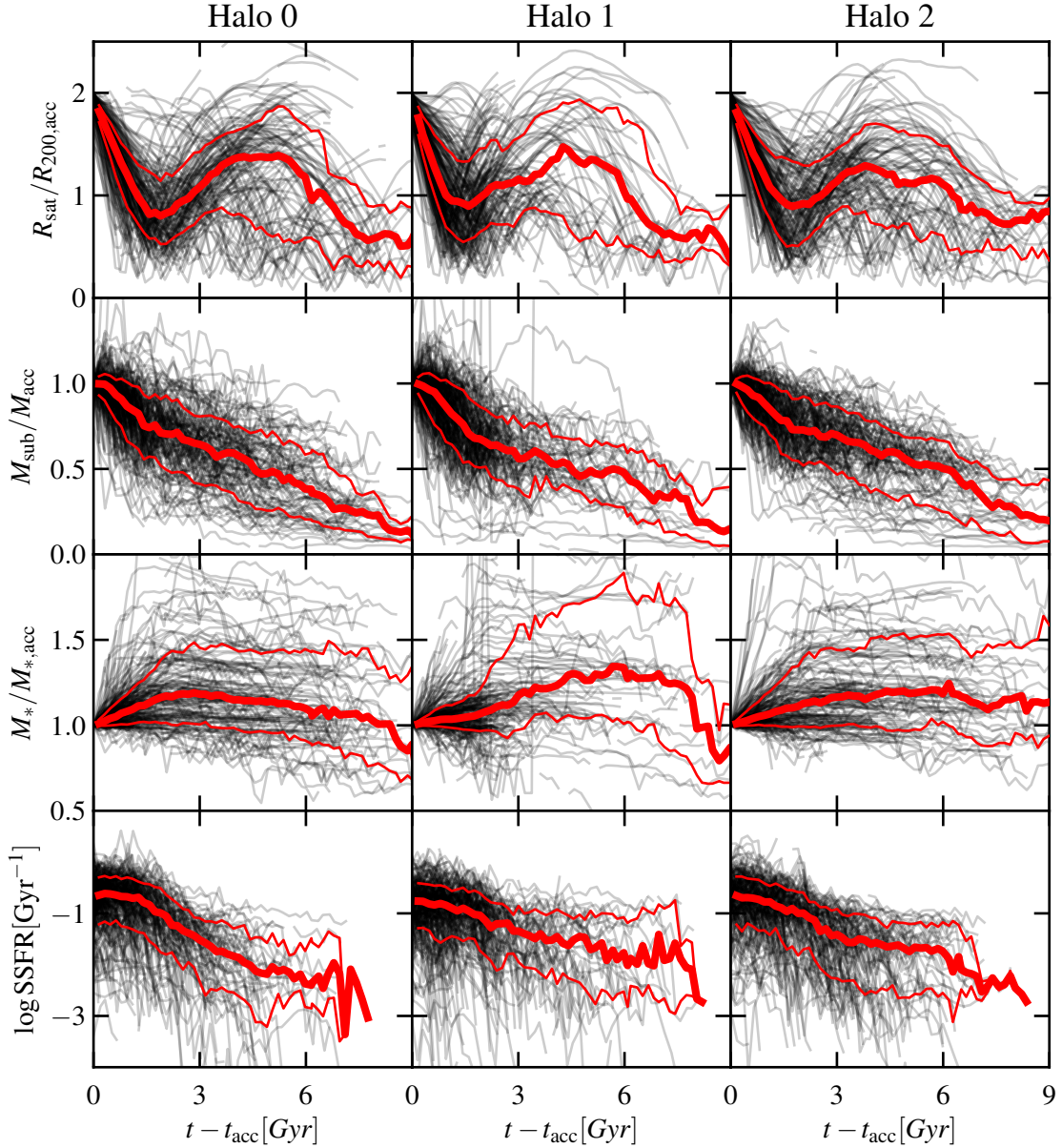


Figure 6. Evolution of subhalo properties as a function of time since accretion: halo-centric distance normalized by the host virial radius at accretion (*top panel*), subhalo dark matter mass normalized by the dark matter mass at accretion (*second panel*), stellar mass normalized by stellar mass at accretion (*third panel*), and specific star formation rate (SSFR) (*bottom panel*). Each column represents one of the cluster-like haloes. The black lines represent the evolution for each subhalo independently, while the thick red line shows the median evolution and the thin red lines the 16th and 84th percentiles.

as the majority of them will be accreted and will end up in the central part of the cluster. One will note that they can already be influenced by the cluster at such distance. In general, subhaloes are following spiraling orbits more or less off-centred, leading them towards the centre of the cluster.

We can also observe the first infall into the cluster where the subhaloes pass close to the centre of the cluster. We measure for each host halo the time at which the average

$R_{\text{sat}}/R_{200,\text{acc}}$ evolution reaches its first minimum: for Halo 0 $t_{\text{min}} = 1.8$ Gyr, for Halo 1 $t_{\text{min}} = 1.5$ Gyr, and for Halo 2 $t_{\text{min}} = 1.7$ Gyr. This first crossing has been discussed in some studies (see for example [Jaffé et al. 2015](#)) as the moment when they are ram-pressure stripped from their gas. We will compare this timescale with the dark matter loss and star formation quenching timescales in the next sections.

4.2 Evolution of the dark matter mass

We now follow the evolution of the subhaloes dark matter content during infall. The top middle panel of Fig. 6 shows the time evolution of the mass of the dark matter particles bound to the subhaloes normalized by the mass at accretion $M_{\text{sub}}/M_{\text{acc}}$ as a function of time. We plot again the evolution for each subhalo and the median value at each time step.

Looking at the median evolution, the mass normalized by the mass at accretion shows a decrease over time, starting very soon after the subhaloes infall at $2 \times R_{200}$. We examine more carefully the mass-loss start time in Sect. 5. There seem to be two different regimes in the mass-loss, with the subhaloes losing matter more rapidly up to $t - t_{\text{acc}} \sim 1.5$ Gyr. To check this trend, we fit a broken line to the mass evolution, to obtain the two slopes of the evolution α_{dm} and β_{dm} , and the time at which the slope changes t_{dm} . The function is defined as:

$$\frac{M_{\text{sub}}}{M_{\text{acc}}}(t) = \begin{cases} \alpha_{\text{dm}}t + c_{\text{dm}}, & \text{if } t < t_{\text{dm}} \\ \beta_{\text{dm}}t + c'_{\text{dm}}, & \text{if } t > t_{\text{dm}} \end{cases} \quad (3)$$

where $c' = (\alpha_{\text{dm}} - \beta_{\text{dm}})t_{\text{dm}} + c_{\text{dm}}$. This is shown in the top panel of Fig. 7. We perform the fit on the median evolution over the subhaloes from the three host haloes. The best fit parameters are presented in Table 5.

The best fit evolution shows a slope change at $t_{\text{DM}} = (1.72 \pm 0.04)$ Gyr: on average subhaloes appear to lose their mass faster during their first infall, with a rate of $\sim 20\%$ of their mass at accretion per Gyr. The mass loss then slows to a rate of $\sim 6\%$ of their mass at accretion per Gyr. As shown in previous studies (eg. Diemand et al. 2007), the subhaloes lose most of their mass at their successive passages at the pericenter, and an even larger fraction at the first passage.

As a comparison we compute a simple analytical model for the subhalo mass loss by tidal stripping. At each time step, the total mass gravitationally bound to the subhalo can be defined as being enclosed in the tidal radius r_t . Beyond this radius, matter is disrupted by the tidal forces of the host halo:

$$F_T = -\frac{d}{dR_{\text{sat}}} \left(\frac{GM_{\text{host}}(R_{\text{sat}})}{R_{\text{sat}}^2} \right) r_t \quad (4)$$

as they are stronger than the subhalo self-gravity:

$$F_G = \frac{GM_{\text{sub}}(r_t)}{r_t^2}, \quad (5)$$

where G is the gravitational constant. For each subhalo and at each time step we compute the value of the tidal radius by solving $F_T = F_G$, assuming that the (sub)haloes follow a Navarro-Frenk-White density profile (NFW, Navarro et al. 1996) to compute the mass. The subhalo mass is then defined as the NFW mass truncated at r_t . The top panel of Fig. 7 shows as a dotted line the evolution of this theoretical value normalized by mass at accretion, averaged over the subhaloes of the three hosts.

The mass loss predicted by this simple analytical model is in very good agreement with the simulation during the first infall, i.e. up to $\sim 2 - 3$ Gyr. However, after that it underestimates the mass loss. This is to be expected with such a simple model, as for instance it does not take into account the possible reorganization of the mass within the subhalo

f_{surv}	$\langle f_{\text{surv}} \rangle$	$\langle t_0 - t_{\text{acc}} \rangle$ (Gyr)
[0, 0.25]	0.15 ± 0.07	7.72 ± 2.11
[0.25, 0.5]	0.40 ± 0.07	5.41 ± 2.10
[0.5, 0.75]	0.62 ± 0.07	3.71 ± 1.80
[0.75, ∞]	0.94 ± 0.21	1.92 ± 1.41

Table 4. Mean surviving mass $f_{\text{surv}} = M_{\text{sub}}(z=0)/M_{\text{sub}}(z_{\text{acc}})$ at redshift $z=0$ and mean time since accretion $t_0 - t_{\text{acc}}$ for subhaloes divided in bins in surviving mass. The error bars represent the standard deviation.

but considers that it keeps following a NFW mass distribution with an abrupt cut at the tidal radius. It is also possible that collisions between satellites play a role in the mass evolution, and they are not included in the simple model (Tormen et al. 1998).

We show in addition in the top panel of Fig. 7 the exponential mass loss in equation 10 in Giocoli et al. (2008). They adopt a different definition for the accretion time, namely the time when the subhalo cross the virial radius of the host halo for the last time, which corresponds in our case to $t - t_{\text{acc}} \sim 6$ Gyr (see top panel of Fig. 6). We also vary the parameter τ_0 from their equation, as the subhaloes survive longer in simulations that include baryons. It appears indeed that the model from Giocoli et al. (2008) describes quite well the evolution that we measure after $t - t_{\text{acc}} = 6$ Gyr when we fix $\tau_0 = 2.5 - 3$ Gyr.

Figure 6 shows that the subhaloes that stay the longest in the host, up to $t = t_{\text{acc}} + 9$ Gyr, appear to lose $\sim 75\%$ of their mass which is well consistent with the shift in the stellar-to-halo mass relation presented in Sect. 3. However, most of the subhaloes at $t = 0$ have not been accreted for such time and have therefore lost less than 75% of their mass. To quantify this effect, we split the subhaloes into four samples according to their surviving mass at $z=0$, $f_{\text{surv}} = M_{\text{sub}}(z=0)/M_{\text{sub}}(z_{\text{acc}})$, and compute for each sample the mean time since accretion. We find as expected that the subhaloes with the lowest surviving mass ($f_{\text{surv}} < 0.25$) have spend the longest time in their host ($t_0 - t_{\text{acc}} \sim 8$ Gyr), while subhaloes with a high surviving mass ($f_{\text{surv}} > 0.75$) have started their infall much more recently ($t_0 - t_{\text{acc}} \sim 2$ Gyr). We summarize the values for each sample in Table 4.

4.3 Stellar mass evolution

We are now looking at the evolution in stellar mass during infall, and investigate if it could in part be responsible for the SHMR shift. In a similar way as for the dark matter mass, we normalize the stellar mass at each epoch by the stellar mass at accretion, and present in the third panel of Fig. 6 the normalized stellar mass as a function of time, for the three host haloes. The median stellar mass is increasing after the subhaloes cross $2 \times R_{200}$, showing that in average galaxies are still star forming at this time.

The median stellar mass then starts to stagnate, showing that the star formation is slowing down after accretion. Similarly as for the dark matter mass, we measure the mean evolution over the three host haloes and fit a broken line to it, defined as in equation 6. The median evolution is presented in the middle panel of Fig. 7, and the best fit parameters are listed in Table 5. The fit indeed shows a transition between a regime where the stellar mass increases (+6% of

All haloes

	M_{DM}	M_*	SSFR
α	-0.192 ± 0.005	0.058 ± 0.001	-0.086 ± 0.018
β	-0.064 ± 0.001	0.003 ± 0.001	-0.366 ± 0.011
γ	—	—	-0.142 ± 0.012
c	1.054 ± 0.004	1.002 ± 0.001	-0.674 ± 0.012
t	1.72 ± 0.05	2.98 ± 0.06	1.21 ± 0.06
t'	—	—	3.32 ± 0.14

Table 5. Best fit parameters of the evolution of the dark matter mass, stellar mass and specific star formation rate (SSFR) as a function of time. The fits are performed on the median evolution over the subhaloes from the three hosts.

the infall mass per Gyr) and a stagnation (+0.3% of the infall mass per Gyr) at $t_* = (2.98 \pm 0.06)$ Gyr.

To see the transition more clearly we show in the bottom panel of Fig. 6 the evolution with time of the Specific Star Formation Rate (SSFR), which is the ratio of the star formation rate and the stellar mass. Among the different definitions of the SFR in Illustris we chose the one compatible with our choice for stellar mass, ie. the sum of the star formation rates of all gas cells within twice the stellar half mass radius of the subhalo. We fit the following function to the SSFR evolution:

$$\frac{M_{\text{ssfr}}}{M_{\text{acc}}}(t) = \begin{cases} \alpha_{\text{ssfr}}t + c_{\text{ssfr}}, & \text{if } t < t_{\text{ssfr}} \\ \beta_{\text{ssfr}}t + c'_{\text{ssfr}}, & \text{if } t_{\text{ssfr}} < t < t'_{\text{ssfr}} \\ \gamma_{\text{ssfr}}t + c''_{\text{ssfr}}, & \text{if } t > t'_{\text{ssfr}} \end{cases} \quad (6)$$

where $c' = (\alpha - \beta)t_{\text{ssfr}} + c$ and $c'' = (\beta - \gamma)t'_{\text{ssfr}} + (\alpha - \beta)t_{\text{ssfr}} + c$.

The evolution of the SSFR shows a clear transition between galaxies that are on average star forming (SSFR $\sim 0.2 \text{ Gyr}^{-1}$) and quenched (SSFR $\sim 0.01 \text{ Gyr}^{-1}$), which happens mostly between $t_{\text{ssfr}} = (1.21 \pm 0.06) \text{ Gyr}^{-1}$ and $t'_{\text{ssfr}} = (3.32 \pm 0.14) \text{ Gyr}^{-1}$. The three different phases are marked by a slope change in the SSFR evolution, with a slower evolution before t_{ssfr} and after t'_{ssfr} than in the transition phase. This transition, happening a few Gyr after the beginning of accretion, is consistent with a slow-starvation delayed-quenching scenario of galaxy evolution in clusters (Tollet et al. 2017).

In summary, looking at Fig. 7 it appears that during the first infall subhaloes loose around 40% of their dark matter at accretion but continue to form stars. Compared to the dark matter stripping, the star formation quenching is delayed, and starts when the subhaloes get closer to the centre of the cluster. We note that we perform the fits presented in Fig. 7 and Table 5 only up to $t - t_{\text{acc}} = 6 \text{ Gyr}$: the small quantity of remaining subhaloes after that time makes the signal much noisier.

In the previous plots all the mass evolution are presented normalized by the mass at accretion. To highlight the relative importance of the dark matter and stellar mass loss we show in Fig. 8 the evolution of the dark matter mass (blue solid line) and the stellar mass (orange dashed line) normalized by the *total* mass at accretion. This shows that the dominating effect on the total mass evolution is the subhalo mass loss, as it represents up to 90% of the mass at accretion, while the stellar mass increase represents only $\sim 1\%$ of the total mass at accretion. However, due to these two effects, the proportion of stellar and dark matter changes drastically during accretion: the ratio of stellar mass to dark mat-

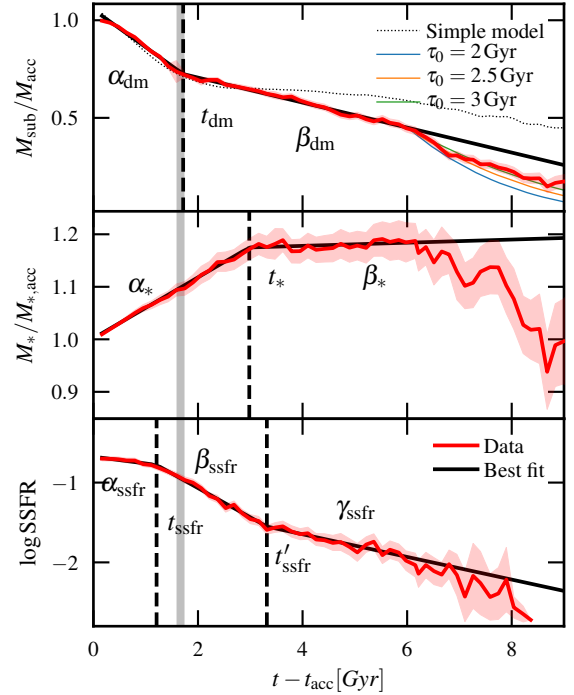


Figure 7. Median evolution of $M_{\text{sub}}/M_{\text{acc}}$ (top panel), $M_*/M_{*,\text{acc}}$ (middle panel) and SSFR (bottom panel) as a function of time (red line, with the error on the median as red filled surfaces) and best fit evolutions (black solid lines). The grey vertical line represents the time at which the mean evolution of the cluster-centric distance reaches its first minimum. The dotted line in the top panel represents the mass evolution for the dark matter stripping simple analytical model (see text for details), and the solid blue, orange and green lines correspond to the subhalo mass loss measured in Giocoli et al. (2008) with $\tau_0 = 2, 2.5$ and 3 Gyr respectively.

ter mass goes from 0.03 to 0.3 during the evolution (black dotted line in Fig. 8).

5 EVOLUTION OF MASS VS R_{SAT}

To have a better representation of the relation between the quenching/stripping and the trajectory of the subhaloes, we look in this section at the evolution of the quantities of interest in this work (dark matter/stellar mass, SSFR) as a function of the distance to the cluster centre. We keep the same subhalo selection as in Sect. 4, and present the evolution for the subhaloes of the three host haloes.

Starting with the dark matter mass, we plot at each time step, starting at their crossing of $2 \times R_{200}$, the position of each subhalo on the $R_{\text{sat}} - M_{\text{sub}}/M_{\text{acc}}$ plane on the top panel of Fig. 9. We also show the median value over all the subhaloes at each time step as a black dot, with the error bars corresponding to the standard error. The dark matter mass appears to remain constant on average until the subhaloes reach $\sim 1.5 \times R_{\text{vir}}$, which would indicate that the subhaloes only start to be affected by their host when they cross some physical boundary of the halo. Such a physical boundary is

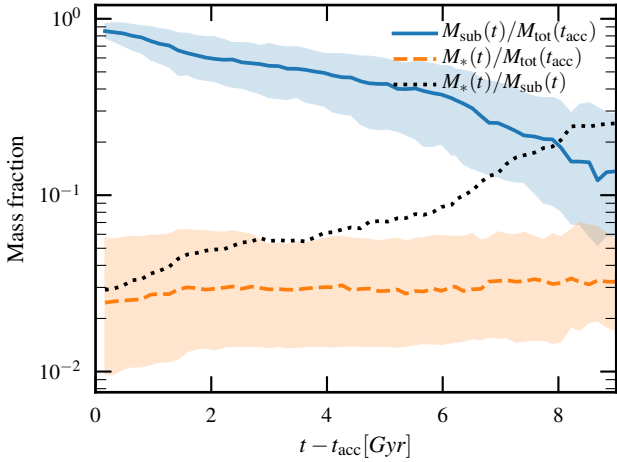


Figure 8. Evolution since the time of accretion of the dark matter mass (solid blue) and the stellar mass (dashed orange) normalized by the *total* mass at accretion. The solid and dashed lines represent the median evolution and the filled surfaces the 68% confidence interval. We show in addition the evolution of the ratio stellar mass to subhalo mass as the black dotted line.

now often considered to be the splashback radius, which is defined as the radius at which accreted matter reaches its first orbital apocenter after turnaround (More et al. 2015b, 2016; Busch & White 2017; Baxter et al. 2017; Diemer et al. 2017). It has been measured to be located at $\sim 1-2 \times R_{\text{vir}}$, which is consistent with what we observe.

The subhaloes then progressively lose their dark matter as they sink towards the centre of the host. Looking at the mean evolution, at the first pericentre $\sim 30\%$ of the dark matter mass is stripped, $\sim 50\%$ after the first orbit, and up to 80% for subhaloes that spend $8-9$ Gyr in their host.

We look now at the evolution of the stellar content of the subhaloes. In the same way as for the dark matter mass, we plot the evolution of the stellar mass as a function of the distance to centre of the host halo on the middle panel of Fig. 9, as well as the evolution of the SSFR on the bottom panel. This representation suggests more clearly how the delay in star formation quenching relates to accretion in the host: on average, during the first infall the satellite galaxies continue to form stars (increase in M_* , SSFR constant), and they start the quenching process after the first passage at the pericentre.

In Smith et al. (2016), they study the stripping of stellar and dark matter in galaxies during their infall into simulated clusters, and found that 18% of the galaxies where undergoing important star formation during accretion, with an increase in stellar mass higher than 15% . We test the influence of strongly star forming galaxies by removing all galaxies that increase their stellar mass by more than 50% during their infall, which represent 10% of the total number of satellite galaxies in our sample. Without them, the slope of the mean stellar mass increase before the first passage at the pericentre is only slightly modified (they reach 108% of their initial stellar mass, instead of 109% for the full sample), but the sharp increase just after the pericentre passage is dampened (maximum stellar mass is 114% of the initial mass, compared to 120% for the full sample at the

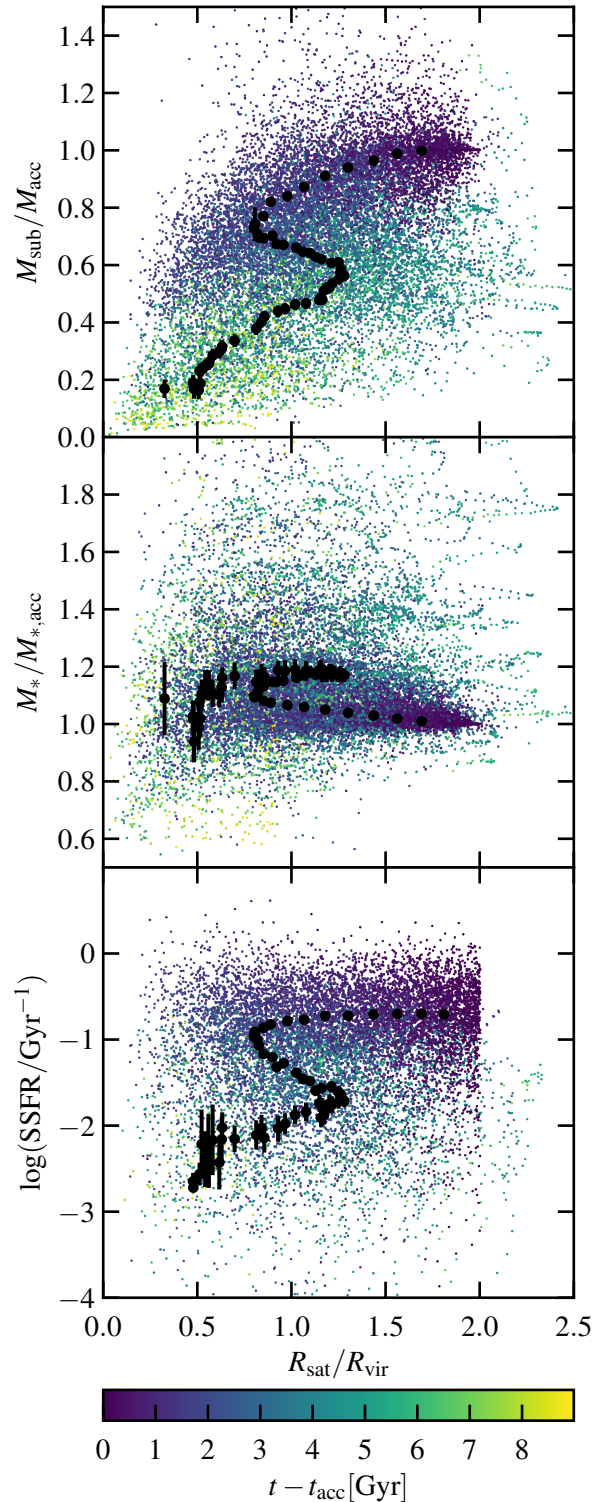


Figure 9. Position of the subhaloes on the $R_{\text{sat}} - M_{\text{sub}}/M_{\text{acc}}$ (top panel), $R_{\text{sat}} - M_*/M_{*,\text{acc}}$ (middle panel) and $R_{\text{sat}} - \text{SSFR}$ plane (bottom panel) at each time step, starting when they are accreted at $2 \times R_{200}$. The color of each point represents the time since accretion. The black dots represent the median values at each time step.

same moment). This could be explained by a small fraction of galaxies experiencing a violent star formation burst, close to their passage at the pericentre: observations of such star formation bursts in infalling galaxies have been reported for example in Gavazzi et al. (2003), who argue that it is caused by enhanced ram-pressure during a high velocity infall.

6 SUMMARY AND DISCUSSION

We present in this analysis a study of the evolution of satellite galaxies during their infall into the three most massive haloes of the Illustris-1 simulation. We first measure the stellar-to-halo mass relation for central galaxies, and find that it is shifted towards lower halo mass compared to the same relation for the satellite galaxies from the simulation. We note that both for haloes and subhaloes, the SHMR that we measure differs at both mass ends from what was measured using abundance matching (Moster et al. 2013; Rodríguez-Puebla et al. 2013), with in particular an excess of massive galaxies that could be explained by an underestimation of AGN feedback in the simulation that fails to properly reduce star formation in massive haloes. It would therefore be interesting to follow up on this work using the IllustrisTNG simulation, which includes a new modeling of both stellar and AGN feedback.

To understand which mechanisms drive the shift of the SHMR for satellite galaxies, we look at the time evolution of the stellar and dark matter mass of the subhaloes during their infall. We find that the subhaloes lose a significant amount of their mass after their accretion by the cluster (at a distance smaller than $\sim 1.5 \times R_{200}$), which is in agreement with the tidal stripping scenario. The quenching of star formation is delayed compared to the dark matter stripping, and galaxies stop on average to form new stars after their first passage within the host core. Around 8 Gyr after accretion, the average stellar mass of the satellite galaxies starts to decrease as well: this could imply that the stellar mass starts to be stripped as well when the subhaloes have only $\sim 30\%$ of their dark matter mass remaining, but it could also be an artifact due to the small number of galaxies that have spent more than 7 Gyr in the clusters.

We summarize the measured evolution of satellite stellar-to-halo mass relation in Fig. 10. The evolution can be divided into three phases: during the first one, which corresponds roughly to the first infall, the galaxies lose on average $\sim 30\%$ of their dark matter mass at accretion and continue to form stars, reaching $\sim 120\%$ of their initial mass (red arrows in Fig. 10). Star formation is then quenched, and the subhaloes continue to lose mass while the stellar mass remains constant (green arrows). Finally, when only 30% of the initial dark matter mass remains, the average stellar mass starts to decrease as well (blue arrows). We note that the evolution represented by the arrows seems to predict a larger evolution of the SHMR than what we measured (dashed line): this is simply due to the fact that not all subhaloes follow this evolutionary path to the end, but are distributed along the way.

Although studies of simulations such as the one presented here allow to disentangle the evolution of the dark and stellar components, it is much more difficult in observational works, and the only observable that can be potentially

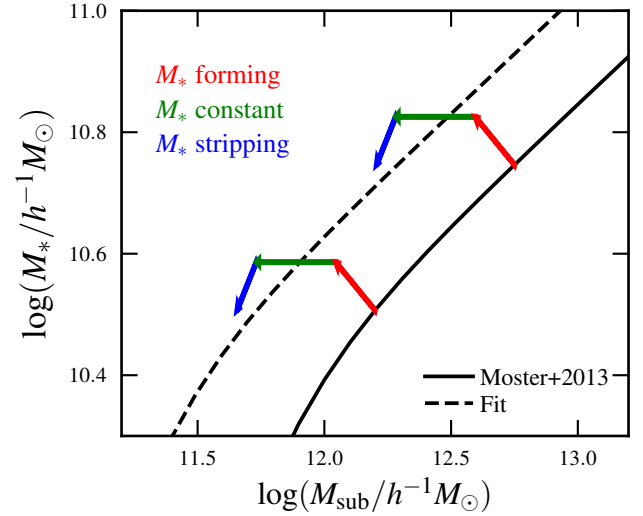


Figure 10. Summary of the subhalo SHMR evolution. The black solid line represents the SHMR for central galaxies at $z = 0$ from Moster et al. (2013), and the dashed line the fit from Sect. 3. The arrows show the three different phases of the evolution: dark matter stripping + star formation in red, dark matter stripping only in green, and dark + stellar matter stripping in blue.

obtained is the stripping factor τ_{strip} which includes both the stripping of dark matter and the formation or stripping of stellar matter. However, if the real evolution is similar to what simulations predict, dark matter stripping should represent the main contribution in the shift of the SHMR. Figure 10 shows that the amplitude of the subhalo mass evolution is ~ 0.6 dex while for stellar mass it is only 0.1 dex. In any case, the stripping of subhaloes (or SHMR shift) has for now not been strongly measured in observations. For instance, weak gravitational lensing allows to statistically measure the total mass of subhaloes, with a precision that is proportional to the area and the depth of the available observations. The advent of large galaxy surveys such as DES or Euclid in the future could therefore allow to put stronger observational constraints on the SHMR shift in clusters.

Another aspect that remains observationally challenging is to estimate the stage of accretion of galaxies in clusters, and even simply their membership. A commonly used proxy is the projected distance to the cluster centre, which is on average indeed correlated with the time since accretion but adds noise coming from the shapes of the individual orbits and from line-of-sight projections.

ACKNOWLEDGEMENTS

MJ was supported by the Science and Technology Facilities Council (grant number ST/L00075X/1). CG acknowledges support from the Italian Ministry of Foreign Affairs and International Cooperation, Directorate General for Country Promotion (Project "Crack the lens"); and the financial contribution from the agreement ASI n.I/023/12/0 "Attività relativa alla fase B2/C per la missione Euclid". ML acknowledges CNRS and CNES for support.

APPENDIX A: CORNER PLOTS**References**

- Bahé Y. M., et al., 2017, *MNRAS*, **470**, 4186
- Baxter E., et al., 2017, *ApJ*, **841**, 18
- Binney J., Tremaine S., 2008, *Galactic Dynamics: Second Edition*. Princeton University Press
- Bluck A. F. L., et al., 2016, *MNRAS*, **462**, 2559
- Brainerd T. G., 2018, preprint, ([arXiv:1810.12914](https://arxiv.org/abs/1810.12914))
- Busch P., White S. D. M., 2017, *MNRAS*, **470**, 4767
- Butcher H., Oemler Jr. A., 1978, *ApJ*, **226**, 559
- Diemand J., Kuhlen M., Madau P., 2007, *ApJ*, **667**, 859
- Diemer B., Mansfield P., Kravtsov A. V., More S., 2017, *ApJ*, **843**, 140
- Dolag K., Borgani S., Murante G., Springel V., 2009, *MNRAS*, **399**, 497
- Dressler A., 1980, *ApJ*, **236**, 351
- Foreman-Mackey D., Hogg D. W., Lang D., Goodman J., 2013, *PASP*, **125**, 306
- Gao L., White S. D. M., Jenkins A., Stoehr F., Springel V., 2004, *MNRAS*, **355**, 819
- Gavazzi G., Cortese L., Boselli A., Iglesias-Paramo J., Vilchez J. M., Carrasco L., 2003, *ApJ*, **597**, 210
- Genel S., et al., 2014, *MNRAS*, **445**, 175
- Giocoli C., Tormen G., van den Bosch F. C., 2008, *MNRAS*, **386**, 2135
- Giocoli C., Tormen G., Sheth R. K., van den Bosch F. C., 2010, *MNRAS*, **404**, 502
- Giocoli C., Tormen G., Sheth R. K., 2012, *MNRAS*, **422**, 185
- Giocoli C., Marulli F., Baldi M., Moscardini L., Metcalf R. B., 2013, *MNRAS*, **434**, 2982
- Gunn J. E., Gott III J. R., 1972, *ApJ*, **176**, 1
- Guo Q., White S., Li C., Boylan-Kolchin M., 2010, *MNRAS*, **404**, 1111
- Guo Q., et al., 2015, *Monthly Notices of the Royal Astronomical Society*, 461
- Hinshaw G., et al., 2013, *ApJS*, **208**, 19
- Jaffé Y. L., Smith R., Candlish G. N., Poggianti B. M., Sheen Y.-K., Verheijen M. A. W., 2015, *MNRAS*, **448**, 1715
- Kauffmann G., White S. D. M., Guiderdoni B., 1993, *MNRAS*, **264**, 201
- Klypin A. A., Trujillo-Gomez S., Primack J., 2011, *ApJ*, **740**, 102
- Klypin A., Yepes G., Gottlöber S., Prada F., Heß S., 2016, *MNRAS*, **457**, 4340
- Li R., et al., 2016, *MNRAS*, **458**, 2573
- Lotz M., Remus R.-S., Dolag K., Biviano A., Burkert A., 2018, preprint, ([arXiv:1810.02382](https://arxiv.org/abs/1810.02382))
- Martinović N., Micic M., 2017, preprint, ([arXiv:1706.04022](https://arxiv.org/abs/1706.04022))
- Merritt D., 1983, *ApJ*, **264**, 24
- Moore B., Katz N., Lake G., Dressler A., Oemler A., 1996, *Nature*, **379**, 613
- Moore B., Lake G., Katz N., 1998, *ApJ*, **495**, 139
- More S., Miyatake H., Mandelbaum R., Takada M., Spergel D. N., Brownstein J. R., Schneider D. P., 2015a, *ApJ*, **806**, 2
- More S., Diemer B., Kravtsov A. V., 2015b, *ApJ*, **810**, 36
- More S., et al., 2016, *ApJ*, **825**, 39
- Moster B. P., Naab T., White S. D. M., 2013, *MNRAS*, **428**, 3121
- Muldrew S. I., Pearce F. R., Power C., 2011, *MNRAS*, **410**, 2617
- Munshi F., et al., 2013, *ApJ*, **766**, 56
- Navarro J. F., Frenk C. S., White S. D. M., 1996, *ApJ*, **462**, 563
- Niemiec A., et al., 2017, *MNRAS*, **471**, 1153
- Oemler Jr. A., 1974, *ApJ*, **194**, 1
- Rodríguez-Gomez V., et al., 2015, *MNRAS*, **449**, 49
- Rodríguez-Puebla A., Avila-Reese V., Drory N., 2013, *ApJ*, **767**, 92
- Rozo E., Rykoff E. S., 2014, *ApJ*, **783**, 80
- Rykoff E. S., et al., 2014, *ApJ*, **785**, 104
- Sales L. V., et al., 2015, *MNRAS*, **447**, L6
- Sawala T., Frenk C. S., Crain R. A., Jenkins A., Schaye J., Theuns T., Zavala J., 2013, *MNRAS*, **431**, 1366
- Schaye J., et al., 2015, *MNRAS*, **446**, 521
- Smith R., Choi H., Lee J., Rhee J., Sanchez-Janssen R., Yi S. K., 2016, *ApJ*, **833**, 109
- Snyder G. F., et al., 2015, *MNRAS*, **454**, 1886
- Somerville R. S., Hopkins P. F., Cox T. J., Robertson B. E., Hernquist L., 2008, *MNRAS*, **391**, 481
- Springel V., 2010, *MNRAS*, **401**, 791
- Springel V., White S. D. M., Tormen G., Kauffmann G., 2001, *MNRAS*, **328**, 726
- Springel V., et al., 2005, *Nature*, **435**, 629
- Srisawat C., et al., 2013, *MNRAS*, **436**, 150
- Terrazas B. A., Bell E. F., Henriques B. M. B., White S. D. M., Cattaneo A., Woo J., 2016, *ApJ*, **830**, L12
- Tollet É., Cattaneo A., Mamon G. A., Moutard T., van den Bosch F. C., 2017, *MNRAS*, **471**, 4170
- Tormen G., Diaferio A., Syer D., 1998, *MNRAS*, **299**, 728
- Tormen G., Moscardini L., Yoshida N., 2004, *MNRAS*, **350**, 1397
- Vogelsberger M., et al., 2014a, *MNRAS*, **444**, 1518
- Vogelsberger M., et al., 2014b, *Nature*, **509**, 177
- Wellons S., et al., 2015, *MNRAS*, **449**, 361
- White S. D. M., Frenk C. S., 1991, *ApJ*, **379**, 52
- Xu D., Springel V., Sluse D., Schneider P., Sonnenfeld A., Nelson D., Vogelsberger M., Hernquist L., 2017, *MNRAS*, **469**, 1824

This paper has been typeset from a \LaTeX file prepared by the author.

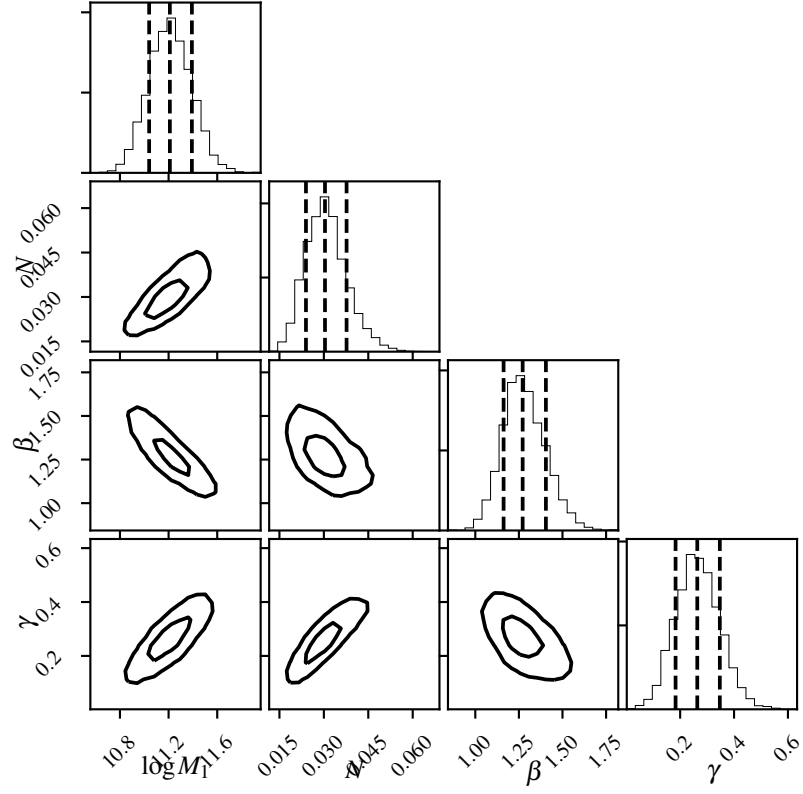


Figure A1. Joint 2-dimensional and marginalized 1-dimensional posterior probability distributions for the SHMR parameters M_1 , N , β and γ fitted to the central galaxies.

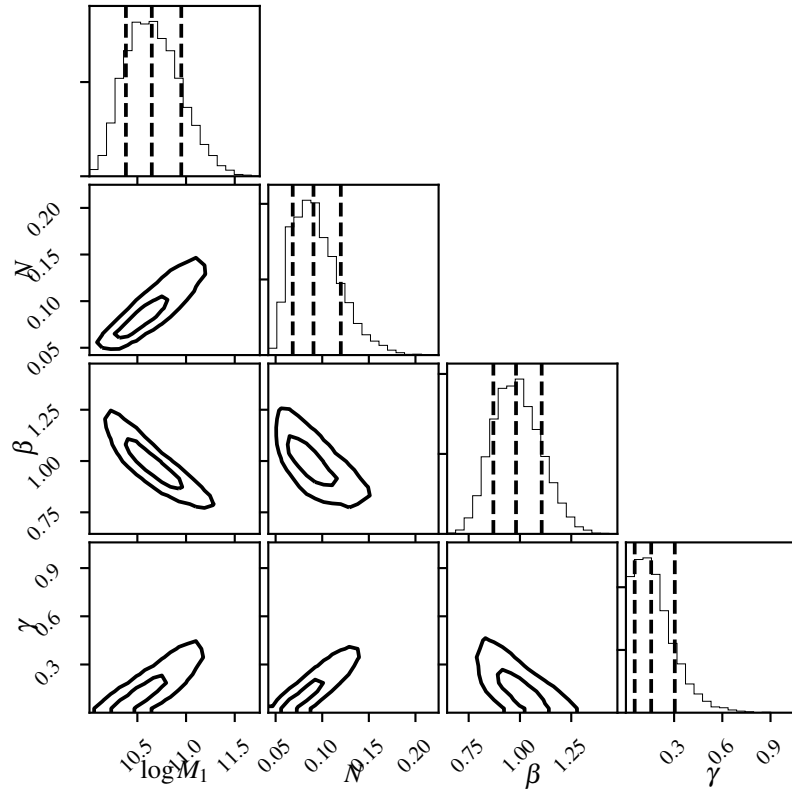


Figure A2. Same as Fig. A1 but for the satellite galaxies.